A Computational Study on Synaptic Plasticity Regulation and Information Processing in Neuron-Astrocyte Networks

Roman Vuillaume, Jhunlyn Lorenzo, Stéphane Binczak, Sabir Jacquir

LETTER **Communicated by Suhita Nadkarni**

A Computational Study on Synaptic Plasticity Regulation and Information Processing in Neuron-Astrocyte Networks

Roman Vuillaume
roman.vuillaume@u-bourgogne.fr
Jhunlyn Lorenzo
Jhunlyn.Lorenzo@u-bourgogne.fr
Stéphane Binczak
stbinc@u-bourgogne.fr
Laboratory ImViA EA 7535, Université Bourgogne, Franche-Comté, 21078 Dijon, France

Sabir Jacquir
sabir.jacquir@u-psud.fr
Université Paris-Saclay, CNRS, Institut des Neurosciences Paris-Saclay, 91190 Gif-sur-Yvette, France

Postsynaptic ionotropic receptors critically shape synaptic currents and underpin their activity-dependent plasticity. In recent years, regulation of expression of these receptors by slow inward and outward currents mediated by gliotransmitter release from astrocytes has come under scrutiny as a potentially important mechanism for the regulation of synaptic information transfer. In this study, we consider a model of astrocyte-regulated synapses to investigate this hypothesis at the level of layered networks of interacting neurons and astrocytes. Our simulations hint that gliotransmission sustains the transfer function across layers, although it decorrelates the neuronal activity from the signal pattern. Overall, our results make clear how astrocytes could transform neuronal activity by inducing a lowfrequency modulation of postsynaptic activity.

1 Introduction

The involvement of glial cells, particularly astrocytes in synaptic activity, has led to considering synapses as tripartite entities, where, along with the pre- and postsynaptic terminal, the perisynaptic astrocyte is an active partner in the modulation of synaptic transmission (Perea, Navarrete, & Araque, 2009). Astrocytes can indeed release neuroactive molecules, dubbed "gliotransmitters," in response to synaptic activity. Gliotransmitters, in turn, modulate synaptic activity and, thereby, synaptic plasticity (De Pittà, Brunel, & Volterra, 2016). The reaction of astrocytes could also facilitate the arrival of new information by modulating the dynamics at

Neural Computation **33, 1970–1992** (2021)
https://doi.org/10.1162/neco_a_01399

Ranvier nodes' level, as suggested by Lorenzo, Vuillaume, Binczak, and Jacquir (2020). Astrocytes' influence reaches the extrasynaptic areas, which induces a modulation of the extrasynaptic depolarization and, once again, synaptic plasticity (Papouin & Oliet, 2014). The boom of artificial intelligence–based technology leads to increased use of spiking neural networks to understand information processing and implement their features in many applications (Delorme, Gautrais, van Rullen, & Thorpe, 1999). Understanding how plasticity reacts and shapes information processing can often lead to critical repercussions in machine learning and artificial intelligence tasks. In this way, astrocyte influence over synaptic and extrasynaptic plasticity appears to be highly relevant in the study of neural computation (Alvarellos-González, Pazos, & Porto-Pazos, 2012; Sajedinia & Hélie, 2018).

A widely regarded learning paradigm, in both the biological and artificial context, is associative Hebbian learning, whereby the correlated firing of pre- and postsynaptic neurons generates positive feedback that increases the strength of the synaptic connection between those neurons (Dayan & Abbott, 2001; Morris, 1999). Indeed, increasing or decreasing the weight of synaptic signaling appears to be convenient when it comes to performing computational tasks. However, postsynaptic plasticity does not exactly follow the Hebbian rule. At the biological level, this reinforcement (or lack thereof) generally depends on activity-dependent modulations of postsynaptic ionotropic transporters. At excitatory synapses, typically one can find α-amino-3-hydroxy-5-methyl-4-isoxazole propionic acid (AMPAR) and N-methyl-D-aspartate receptors (NMDAR). These receptors are known to be numerous in the cortical pyramidal neuron (Abbott & Nelson, 2000). Synaptic activity causes an increase in the concentration of calcium in the postsynaptic button. This increase stimulates the traffic of the ionotropic receptors, which than can be targeted by the neurotransmitters. AMPAR, which contains GluA2 protein, are known to be numerous in the cortical pyramidal neurons and impermeable to Ca^{2+} in the mature brain (Wright & Vissel, 2012; Morita, Rah, & Isaac, 2013). This implies that their main contribution is the depolarization of the postsynaptic membrane, which eases the lifting of an Mg^{2+} block of NMDAR. The activation of NMDAR and voltage-gated calcium channel (VGCC) is the main contribution in Ca^{2+} concentration (Malenka & Bear, 2004). When the NMDA receptors move to extrasynaptic areas, they switch from presynaptic to astrocytic influence (Papouin & Oliet, 2014). Gliotransmission contributes to depolarize the dendritic compartment's membrane. This leads to postsynaptic ionotropic receptors' opening through coupling conductance.

Glial cells can also form a network. Interastrocyte communication seems to be only chemical (Scemes & Giaume, 2006), as astrocytes do not display action potential generation. In the astrocyte's network, astrocyte's territory is nonoverlapping (Bushong, Martone, Jones, & Ellisman, 2002). However, the strictly chemical communication known as slow inward current (SIC) could induce delayed and slower influence of the astrocyte's network to

any linked synapse, which can be hard to study if the focus is only on the neuron. Considering that synaptic plasticity depends on postsynaptic membrane potential and that astrocyte-mediated SICs modulate this activity indirectly, this work focuses on the involvment of gliotransmission on AMPAR trafficking. In particular, the dynamics of the model for tripartite synapse proposed by Stimberg, Goodman, Brette, and Pittà (2019) have been enriched. This model distinguishes between intra- and extrasynaptically located postsynaptic receptors. In a recent review, Kastanenka et al. (2020) also considered how astrocytes modulate information processing. The slow Ca^{2+} oscillation taking place in astrocytes makes them attuned for slow dynamics. However, they may predominantly modulate fast neuronal activity (Perea et al., 2016; Sardinha et al., 2017). Lenk et al. (2020) investigated astrocyte's connectivity influence over noisy neuronal activity. They showed that gliotransmission's homeostatic effect decreases high neuronal activity and increases low neuronal activity. Though this homeostatic influence appears critical, we intend to test the astrocytic signaling impact on neuronal networks with various activities. We aim to perform a step further toward signal processing by studying how a neuron-astrocyte network processes an activity pattern. In this study, we investigate the gliotransmission's influence on several varying frequencies of signal patterns processing. Then we consider how astrocytic gliotransmission modulates AMPAR trafficking and the overall neuronal activity.

2 Method

This research is based on the modelization on several studies, which contributed to different neural and astrocyte modeling. Though we tried to implement the equations as close as possible to the original works, we adapted some parameters to study neuron-astrocyte network activity. The postsynaptic bouton's dynamics is based on Tewari and Majumdar (2012), the AMPAR trafficking on Shouval, Castellani, Blais, Yeung, and Cooper (2002), the dendritic compartment on Kepecs and Raghavachari (2002), the neuron on Izhikevich (2003), and the astrocyte on Stimberg, Goodman et al. (2019). The implementation details and parameter justification are in the corresponding subsection. The latter study provided the simulation code for astrocyte's dynamics. We based our simulation code on theirs and consider that the overall model extends theirs.

2.1 Neuron Model. A two-compartment model of neurons is considered with the soma and the dendritic arbor. The dendritic compartment model is conductance based, while the neuron model is phenomenological. This adaptation preserves neuronal dynamics for a large span of input current dynamics (i.e., applied current and synaptic input) and stability regarding the time step of differential equations. Somatic neuronal dynamics are defined using the model of neocortical pyramidal neuron proposed by

Izhikevich (2003):

$$C\frac{dV_s}{dt} = k(V_s - V_{rest})(V_s - v_t) - u + I + \chi \tag{2.1}$$

$$\frac{du}{dt} = a(b(V_s - V_{rest}) - u) \tag{2.2}$$

$$\text{if } V_s \geq V_\theta, \textit{then} \begin{cases} V_s = c \\ u = u + d, \end{cases} \tag{2.3}$$

where V_s is the membrane potential, u the recovery parameter, and a, b are parameters that shape the sensibility of v and u, while c is the reset potential and d the outward-inward currents. All parameter values are depicted in Table 1.

The input current I in equation 2.1 is defined as

$$I = \frac{g_c}{P}(V_d - V_s)A_{soma}. \tag{2.4}$$

We added a random Poisson stimulation (χ) to simulate random neuronal spiking activity around 1 Hz. There is only one dendritic compartment. The dendritic compartment has been implemented following the study of Kepecs and Raghavachari (2002). We assume that the dendrite has a length of 500 μm. This value is based on Fiala, Spacek, and Harris (1999). Given that there is no maximal extent reported for pyramidal neurons, the value is the average of all maximal extent reported. This parameter scales the synaptic input to the dendritic compartment (regarding the synaptic density reported further) and does not affect the results. The dendritic compartment is active, and the membrane potential V_d is estimated by solving

$$\begin{aligned} C_m\frac{dV_d}{dt} &= -I_{Leak} - I_{NaP} - I_{Ks} - I_{KA} \\ &\quad + \frac{g_c}{1-P}(V_s - V_d) \\ &\quad - I_{syn} - I_{extrasyn}, \end{aligned} \tag{2.5}$$

with g_c the coupling conductance between the somatic and the dendritic compartments (Kepecs & Raghavachari, 2002). The persistent sodium current reads

$$I_{NaP} = g_{Na}r_\infty^3(V_d - V_{Na}), \tag{2.6}$$

$$r_\infty = \frac{1}{1 + \exp(-(V_d + 57)/5)}, \tag{2.7}$$

Table 1: Parameters of Neuron and Dendrite Equations.

Symbol	Description	Value	Unit	[Ref.]
C	Somatic membrane potential capacitance	100	pF	[13]
V_{rest}	Somatic membrane resting state	-70	mV	[13*]
k	Constant $\frac{1}{R}$	0.7	$pA.mV^{-1}$	[13]
v_t	Instantaneous threshold potential	-50	mV	[13*]
v_θ	Threshold potential	30	mV	[13*]
a	Recovery time constant	0.03	ms^{-1}	[13]
b	Constant $\frac{1}{R}$	-2	nS	[13]
c	Potential reset value	-60	mV	[13*]
d	Outward - inward currents	100	pA	[13]
K_p	Steepness of neurotransmitter release function	5	mV	[9]
V_p	Value at which the function is half-activated	2	mV	[9]
C_m	Dendrite membrane capacitance	1	$\mu F.cm^{-2}$	[17]
g_c	Soma-dendrite coupling conductance	0.2	$\mu A.cm^{-2}$	[17*]
Mg^{2+}	Magnesium block	1	mM	[9]
d_{spine}	Spine density, assuming 2 per μm	7.96.e+5	cm^{-2}	*
P	Dendrite-soma surface's ratio	0.1		[17]
g_{Na}	Sodium channel conductance	0.25	$mS.cm^{-2}$	[17]
g_{Ks}	Potassium channel conductance	0.1	$mS.cm^{-2}$	[17]
g_{KA}	Potassium channel conductance	10	$mS.cm^{-2}$	[17]
g_{AMPAR}	AMPAR conductance	0.35–1.0	nS	[9]
g_{NMDAR}	NMDAR conductance	0.01–0.6	nS	[9]
g_{eNMDAR}	Extrasynaptic NMDAR conductance	0.01–0.6	nS	[9]
g_{GABAR}	GABAR conductance	0.25	nS	[9]
V_{Na}	Reversal potential	-55	mV	[17*]
V_K	Reversal potential	-80	mV	[17*]
V_L	Reversal potential	-80	mV	[17*]
V_{AMPAR}	Reversal potential	0	mV	[9]
V_{NMDAR}	Reversal potential	0	mV	[9]
V_{GABAR}	Reversal potential	-70	mV	[9]
α_{AMPAR}	Binding rate	1.1	$\mu M^{-1}ms^{-1}$	[9]
β_{AMPAR}	Unbinding rate	0.19	ms^{-1}	[9]
α_{NMDAR}	Binding rate	0.072	$\mu M^{-1}ms^{-1}$	[9]
β_{NMDAR}	Unbinding rate	0.0066	ms^{-1}	[9]
α_{eNMDAR}	Binding rate	0.072	$\mu M^{-1}ms^{-1}$	[9]
β_{eNMDAR}	Unbinding rate	0.0066	ms^{-1}	[9]
α_{GABAR}	Binding rate	5	$\mu M^{-1}ms^{-1}$	[9]
β_{GABAR}	Unbinding rate	0.18	ms^{-1}	[9]

Notes: Ref. number identification: 9: Destexhe, Mainen, & Sejnowski, 1998; 13: Izhikevich, 2003; 17: Kepecs & Raghavachari, 2002. *: Experimentally adjusted.

and the two potassium currents

$$I_{Ks} = g_{Ks} q_\infty (V_d - V_K), \tag{2.8}$$

$$q_\infty = \frac{1}{1 + \exp((V_d + 60)/10)}, \tag{2.9}$$

$$I_{KA} = g_{KA} a_\infty^3 b_\infty (V_d - V_K), \tag{2.10}$$

$$a_\infty = \frac{1}{1 + \exp(-(V_d + 45)/6)}, \tag{2.11}$$

$$b_\infty = \frac{1}{1 + \exp(-(V_d + 56)/15)}, \tag{2.12}$$

the leak current

$$I_{leak} = g_{leak}(V_d - V_L), \tag{2.13}$$

with I_{syn} the sum of current from the ith spine head and $I_{extrasyn}$ the sum of current from the extrasynaptic area near the ith spine head:

$$I_{syn} = \sum_{i=1}^{N_{syn}} d_{spine}(I_{NMDAR_i} + I_{AMPAR_i} + I_{GABAR_i}), \tag{2.14}$$

$$I_{extrasyn} = \sum_{i=1}^{N_{syn}} d_{spine} I_{eNMDAR_i}, \tag{2.15}$$

with N_{syn} the number of synapses (20 in this study) and d_{spine} the spine density of a section of the dendritic compartment (i.e., with as much cross-section as synaptic's connection). The current in equations 2.14 and 2.15 is estimated as

$$I_x = g_x m_x B(V_{spine})(V_{spine} - V_x), \tag{2.16}$$

and the ratio of receptors in the open state depends on the neurotransmitters' or gliotransmitters' concentration:

$$\frac{dm_x}{dt} = \alpha_x.[T].(1 - m_x) - \beta_x.m_x, \tag{2.17}$$

$$[T] = \begin{cases} [T](V_{pre}) \text{ if AMPAR, NMDAR, GABAR} \\ G_A \text{ if eNMDAR.} \end{cases} \tag{2.18}$$

with $x =$ AMPAR, NMDAR, eNMDAR, GABAR (see Table 1 for the parameters' values), and the magnesium block for NMDAR, eNMDAR current (Jahr & Stevens, 1990) can be expressed, such as

$$B(V_{spine}) = \frac{1}{1 + \exp(-0.062 V_{spine}) \frac{[Mg^{2+}]}{3.57}}. \tag{2.19}$$

Though the magnesium concentration (i.e., $[Mg^{2+}]$) could vary, in this study we use a fixed value of 1 mM (see Table 1). Otherwise, $B(V_{spine}) = 1$ for equation 2.16 (i.e., for AMPAR and GABAR).

In order to compute with large dt and to avoid computational instability, we fixed $V_{spine} = V_d$. Thus, we assume that in the mean time of one time step, V_{spine} and V_d membrane potentials reached the same value.

2.2 Neurotransmitter Release. To ease the computation, we use the estimation of neurotransmitter release given by Destexhe, Mainen, and Sejnowski (1998),

$$[T](V_{pre}) = \frac{T_{\max}}{1 + \exp(-(V_{pre} - V_p)/K_p)}, \tag{2.20}$$

where $T_{\max}$ is the maximal concentration of neurotransmitter in the synaptic cleft, V_{pre} the presynaptic neuron's voltage, and K_p and V_p can be found in Table 1.

2.3 Synaptic Plasticity. Synaptic plasticity is based on the study of Shouval et al. (2002). For simplicity, we only modeled the density expression of AMPAR (i.e., N_{AMPAR}).

$$\frac{dN_{AMPAR}}{dt} = \frac{\Omega - N_{ampar}}{\tau}, \tag{2.21}$$

with

$$\Omega = 1 - \frac{1}{0.4\sqrt{2\pi}}.\exp\left(-0.5\left(\frac{Ca_{post} - 0.3}{0.25}\right)^2\right), \tag{2.22}$$

$$\tau = \frac{0.14}{1.2 + Ca_{post}^{0.61}}, \tag{2.23}$$

where equations 2.22 and 2.23 give the fixed point and the convergence time for equation 2.21. Though the Ω function's equation is not reported in Shouval et al. (2002), the authors underlined that a function with similar property wouldn't alter the plasticity dynamics (see Figure 1). As $0 \leq N_{AMPAR} \leq 1$, it modifies the value for g_{AMPAR} in equation 2.16:

$$g_{AMPAR} = 0.35 + 0.65N_{AMPAR}. \tag{2.24}$$

which fits in the range reported in Table 1.

The postsynaptic Ca^{2+} (denoted Ca_{post}) dynamics read (Tewari & Majumdar, 2012)

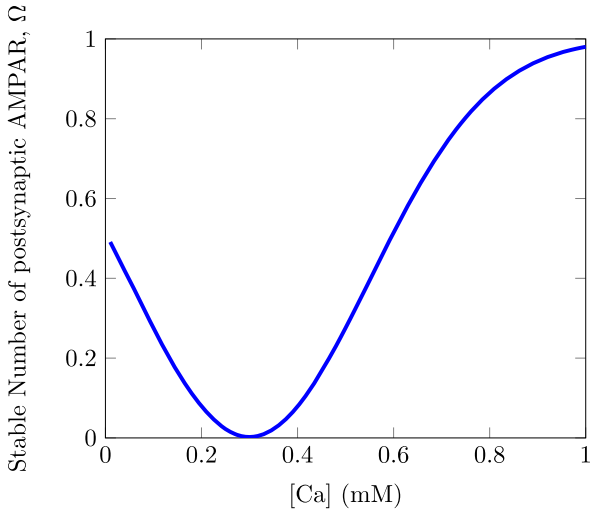

Figure 1: Illustration of Ω as function of spine head's Ca^{2+} concentration.

$$\frac{dCa_{post}}{dt} = \frac{f(Ca_{post})}{1+\theta}, \tag{2.25}$$

where $f(Ca_{post})$ includes membrane proteins, VGCC, and plasma membrane calcium-dependent ATPases (PMCAs) responsible for the Ca^{2+} influx and efflux such as

$$f(Ca_{post}) = -\frac{\eta I_{NMDA} + i_R}{2F v_{spine}} - s_{pump}, \tag{2.26}$$

$$\theta = \frac{b_t K_{endo}}{K_{endo} + {Ca_{post}}^2}, \tag{2.27}$$

$$i_R = g_R B(N_R, P_o)(V_{spine} - V_R), \tag{2.28}$$

$$s_{pump} = k_s(Ca_{post} - Ca_{post}^{rest}), \tag{2.29}$$

where i_R and s_{pump} account for influx and efflux, respectively, and $B(N_R, P_o)$ is a binomially distributed random number describing the VGCC open probability, whenever V_{spine} is greater than activation threshold (i.e., −30 mV, Tewari & Majumdar, 2012; see Table 2 for parameters' values). We did not model Ca^{2+} diffusion between the postsynaptic spine head and the dendritic compartment because this dynamic appeared to be unstable with the time step used in the simulations. In this study, the astrocytic influence is only made through NMDAR-induced depolarization of the dendritic compartment.

Table 2: Parameters of Synaptic Plasticity Model Equations

Symbol	Description	Value	Unit	[Ref.]
η	Fraction of Ca^{2+} current carried by NMDAR	0.057		[33]
P_o	VGCC open probability	0.52		[29]
K_{endo}	Ca^{2+} affinity of Endogenous buffer	10	μM	[16]
b_t	Total endogenous buffer concentration	200	μM	[39]
V_R	Reversal potential of Ca^{2+} ion in spine	27.4	mV	[36]
v_{spine}	Volume of dendrite spine	0.9048	μm^3	[39]
Ca^{rest}_{post}	Resting postsynaptic Ca^{2+} concentration	100	nM	[39]
k_s	Maximum PMCa efflux rate	100	s^{-1}	[16]
g_R	Conductance of R-type channel	15	pS	[29]
N_R	Number of R-type channels	6		[29]

Note: Ref. number identification: 16: Keller, Franks, Bartol, & Sejnowski, 2008; 29: Sabatini & Svoboda, 2000; 33: Schneggenburger, Tempia, & Konnerth, 1993; 36: Sochivko et al., 2002; 39: Tewari & Majumdar, 2012.

2.4 Astrocyte Model. We have used the G-ChI model for astrocyte Ca^{2+} dynamics (Li & Rinzel, 1994; Shuai & Jung, 2002). According to the study by Stimberg, Goodman et al. (2019), the astrocyte Ca^{2+} (denoted Ca) is estimated as

$$\frac{dCa}{dt} = J_r + J_l - J_p, \tag{2.30}$$

$$\frac{dh}{dt} = \frac{h_\infty - h}{\tau_h}(1 + \xi(t)\sqrt{\tau_h}), \tag{2.31}$$

with $\xi(t)$ a white noise and where

$$J_r = \Omega_C a m_\infty^3 h^3 (Ca_T - (1 + \varrho_A)Ca), \tag{2.32}$$

$$J_l = \Omega_L (Ca_T - (1 + \varrho_A)Ca), \tag{2.33}$$

$$J_p = O_P \mathcal{H}_2(Ca, K_P), \tag{2.34}$$

with

$$m_\infty = \mathcal{H}_1(Ca, d_5)\mathcal{H}_1(IP_3, d1), \tag{2.35}$$

$$h_\infty = d_2 \frac{IP_3 + d_1}{d_2(IP_3 + d_1) + (I + d_3)Ca}, \tag{2.36}$$

$$\tau_h = \frac{IP_3 + d_3}{\Omega_2(IP_3 + d_1) + O_2(I + d_3)Ca}, \tag{2.37}$$

and the astrocytic inositol 1,4,5-trisphosphate (denoted IP_3) is estimated as (De Pittà, Goldberg, Volman, Berry, & Ben-Jacob, 2009; Goldberg, De Pittà,

Volman, Berry, & Ben-Jacob, 2010):

$$\frac{dIP_3}{dt} = J_\beta + J_\delta - J_{3K} - J_{5P} + J^i_{net}, \tag{2.38}$$

$$J_\beta = O_\beta \Gamma_A, \tag{2.39}$$

$$J_\delta = O_\delta \frac{\kappa_\delta}{\kappa_\delta + IP_3} \mathcal{H}_2(Ca, K_\delta), \tag{2.40}$$

$$J_{3K} = O_{3K} \mathcal{H}_4(Ca, K_D) \mathcal{H}_1(IP_3, K_3), \tag{2.41}$$

$$J_{5P} = \Omega_{5P} IP_3, \tag{2.42}$$

with $\mathcal{H}$ the Hill function $\mathcal{H}_n(x, K) = \frac{x^n}{x^n + K^n}$, and J^i_{net} is the IP_3 diffusion from neighboring astrocytes, estimated as

$$J^i_{net} = \sum_{j=1}^{NA(i)} -\frac{F_A}{2} \left(1 + \frac{\Delta_{ij} IP_3}{|\Delta_{ij} IP_3|} \tanh\left(\frac{|\Delta_{ij} IP_3| - IP_3^\theta}{IP_{3_{scale}}}\right)\right), \tag{2.43}$$

where $NA(i)$ represents the number of astrocytes neighbor of the ith astrocyte. The fraction of activated astrocyte receptors (see equation 2.39) reads (Wallach et al., 2014):

$$\frac{d\Gamma_A}{dt} = O_N [T]_i (1 - \Gamma_A) - \Omega_N (1 + \zeta \mathcal{H}_1(Ca, K_{KCa})) \Gamma_A, \tag{2.44}$$

where $[T]_i$ is the released glutamate concentration, summed over all synapses managed by the i^{th} astrocyte. See Table 3 for parameter details and values.

2.5 Gliotransmission. The gliotransmitter's available and released resources (see equations 2.17 and 2.18) are estimated as (De Pittà, Volman, Berry, & Ben-Jacob, 2011):

$$\frac{dx_A}{dt} = \Omega_A (1 - x_A), \tag{2.45}$$

$$\frac{dG_A}{dt} = \Omega_e G_A, \tag{2.46}$$

which are updated when astrocytic Ca^{2+} concentration crosses the threshold Ca_θ (see Table 4) (Stimberg, Goodman et al., 2019):

$$G_A \leftarrow G_A + \rho_e G_T U_A x_A, \tag{2.47}$$

$$x_A \leftarrow x_A (1 - U_A), \tag{2.48}$$

Table 3: Parameters of Astrocyte's Equations.

Symbol	Description	Value	Unit	[Ref.]
Ca_T	Total cell free Ca^{2+} content	2	μM	[38]
ρ_a	ER to cytoplasm volume ratio	0.18		[38]
d_1	IP_3 association constant	0.13	μM	[38]
d_2	Ca^{2+} inactivation dissociation constant	1.05	μM	[38]
d_3	IP_3 dissociation constant	0.9434	μM	[38]
d_5	Ca^{2+} activation dissociation constant	0.08	μM	[38]
O_2	IP_3R binding rate of Ca^{2+} inhibition	0.2	μMs^{-1}	[38]
$\Omega_C a$	Maximal rate of Ca^{2+} release by IP_3Rs	6	s^{-1}	[38]
Ω_L	Maximal rate of Ca^{2+} leak from the ER	0.1	s^{-1}	[38]
O_P	Maximal Ca^{2+} uptake rate by SERCAs	0.9	μMs^{-1}	[38]
K_P	Ca^{2+} affinity of SERCAs	0.05	μM	[38]
O_β	Maximal rate of IP_3 production by PLCβ	0.5	μMs^{-1}	[38]
O_δ	Maximal rate of IP_3 production by PLCδ	0.6	μMs^{-1}	[38]
κ_δ	Inhibition constant of PLCδ by IP_3	1.5	μM	[38]
K_δ	Ca^{2+} affinity of PLCδ	0.1	μM	[38]
O_{3K}	Maximal rate of IP_3 degradation by $IP_3 - 3K$	4.5	μMs^{-1}	[38]
K_{3K}	IP_3 affinity of $IP_3 - 3K$	1	μM	[38]
K_D	Ca^{2+} affinity of $IP_3 - 3K$	0.7	μM	[38]
Ω_{5P}	Maximal rate of IP_3 production by $IP5P$	0.05	s^{-1}	[38]
O_N	Agonist binding rate	0.3	$\mu M^{-1}s^{-1}$	[38]
Ω_N	Maximal inactivation rate	0.5	s^{-1}	[38]
K_{KCa}	Ca^{2+} affinity of PKC	0.5	μM	[38]
ζ	Maximal reduction of receptor affinity by PKC	10		[38]
F_A	GJC IP_3 permeability	2	μMs^{-1}	[18]
IP_3^θ	Threshold gradient for IP_3 diffusion	0.3	μM	[38]
$IP_{3_{scale}}$	Scaling factor of diffusion	0.05	μM	[38]

Note: Ref. number identification: 18: Lallouette, De Pittà, & Berry, 2019; 38: Stimberg, Goodman et al., 2019.

2.6 Network Setups. In this study, we modeled a column of pyramidal neurons. The network consisted of three layers of 100 neurons each. In those 100 neurons, 20 were inhibitory interneurons, which connected only to neurons within the same layer. All neurons received 20 synaptic connections. Neurons received around 80% of the synaptic connections from the previous layer to prevent the signal from vanishing through layers and 20% of the synaptic connections from neighbor neurons. The connections were randomly chosen.

There were equal numbers of astrocytes and neurons. Each astrocyte was paired with one postsynaptic neuron, meaning it connected with all the neuron's synapses. Astrocyte-to-astrocyte connectivity depended on the grid's position, following the implementation of Stimberg, Goodman et al. (2019). Each astrocyte could thus make a maximum of four connections (the previous layer astrocyte, the two neighbors of the same layer, and the

Table 4: Parameters of Gliotransmission Equations.

Symbol	Description	Value	Unit	[Ref.]
Ca_θ	Ca^{2+} threshold for exocytosis	0.19669	μM	[39]
G_T	Total vesicular gliotransmitter concentration	250	μM	[11]
Ω_A	Gliotransmitter recycling rate	1.25	s^{-1}	[11; 38; 39*]
U_A	Gliotransmitter release probability	0.6		[38]
ρ_e	Astrocytic vesicle-to-extracellular volume ratio	0.00065		[38]
Ω_e	Gliotransmitter clearance rate	10	s^{-1}	[11; 38; 39*]

Note: Ref. number identification: 11: Flanagan, McDaid, Wade, Wong-Lin, & Harkin, 2018; 38: Stimberg, Goodman et al., 2019; 39: Tewari & Majumdar, 2012. *: Experimentally adjusted.

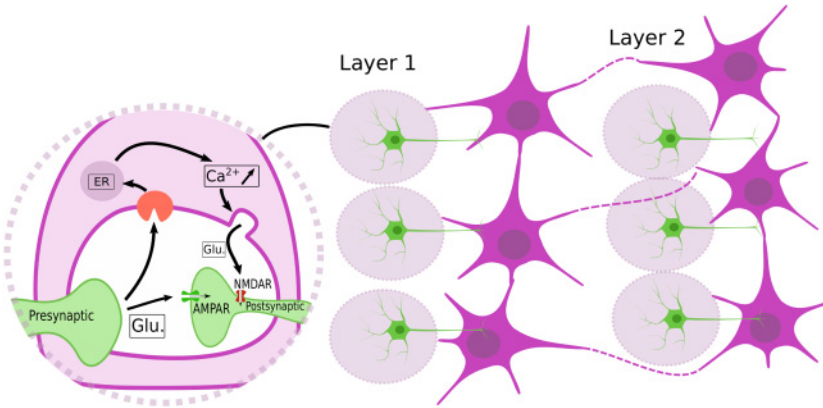

Figure 2: Schematic representation of the astrocytes' nonoverlapping areas and astrocyte-to-astrocyte connectivity.

next-layer astrocyte). A simplified version of the astrocyte-to-astrocyte connectivity is displayed in Figure 2.

2.7 Numerical Method. For the differential equations, we used the forward Euler method, with $dt = 0.1$ ms. The program was written in Python, under the BRIAN2 simulator (Stimberg, Brette, & Goodman, 2019), based on the Stimberg, Goodman et al. (2019) study. For each combination corresponding to the cases «*with astrocyte*», «*without astrocyte*» and «*switch frequency*» condition, we performed 30 simulations. The simulations were carried out on the cluster of the Computing Center of the University of Burgundy (Linux 64 bits, processors Intel Xeon E5-2640v3 (2P, 8C/P). The code can be found at http://modeldb.yale.edu/266794.

2.8 Stimulation and Conditions of Simulation. Since the earliest observation of the relationship between the mean and the variance of neural

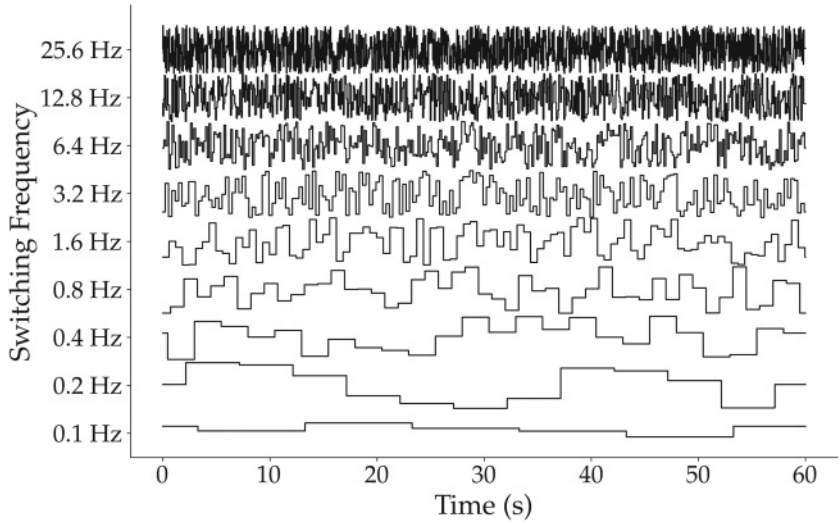

Figure 3: Random stimulation signal generated at several switch frequencies.

responses (Werner & Mountcastle, 1965; Tolhurst, Movshon, & Thompson, 1981), Poisson statistics has often been used to describe the neural firing patterns, so we followed the classic rejection method to generate Poisson spike trains. A step signal of varying intensity drove the frequency of the input neurons' (i.e., 80 excitatory neurons, which make synapses with the first-layer neuronal population) spike trains. The random signal had several variations. We labeled the number of changes as switching frequency, that is, the number of step variations of the signal. The target number of step variations defined the equal duration of each discrete state (e.g., 0.1 Hz switching frequency: 10 s for each discrete state). An example of a random signal pattern for all switching frequency is depicted in Figure 3. The signal pattern drove the firing frequency of an input population of simple neurons (see equation 2.1, in which the frequency of the random Poisson term depends on the step signal's state), which makes synaptic connections with the first layer. An example of the resulting activity is depicted in Figure 4 in the "Neuronal Activity" column.

In this study, we are interested in the astrocytic influence on neuronal dynamics and plasticity. Our simulations compare «*with astrocyte*» and «*without astrocyte*» conditions. However, as astrocytes appear to be the main protagonist in extrasynaptic signaling, there could be an imbalance in the ionotropic receptors' density, particularly in NMDAR maximal conductance. To keep a fair comparison between the two conditions, we fixed the extrasynaptic NMDAR conductance (only effective in the «*with astrocyte*» condition) at the maximal conductance described by Destexhe et al. (1998)

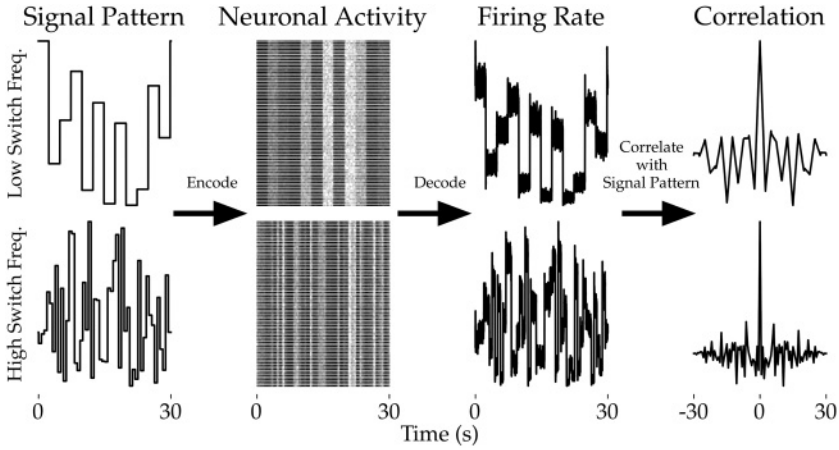

Figure 4: The method used to encode and decode the signal processing through the network.

(i.e., $g_{\max}$). As the minimal NMDAR conductance is 0.01 nS, it would be much lower than the lowest AMPAR conductance (0.35 nS). The NMDAR contribution to the postsynaptic depolarization would be too low to induce any significant change. The maximal NMDAR conductance is 0.6 nS, between the minimal and the maximal AMPAR conductance (0.35 nS to 1 nS), making its contribution to the postsynaptic depolarization meaningful. The synaptic NMDAR conductance was

$$g_{NMDAR} = \begin{cases} 2g_{\max}, \textit{without astrocyte} \\ g_{\max}, \textit{with astrocyte}. \end{cases} \tag{2.49}$$

In this study, we fixed the randomness of each code to perform paired simulation for the «*without astrocyte*» and «*with astrocyte*» conditions (i.e., in each pair of simulation, connectivity, signal, and noise were the same for both conditions). We performed 30 independent simulations for each «*switch frequency*» level (i.e., 9 levels; see Figure 3).

2.9 Parameter Analysis. In this study, we recorded several simulation variables to analyze glial cells' influence over the network activity. Then we used the following measures:

- AMPAR density: Average expression of the AMPAR density for a neuron's synapses, averaged over the neuronal population layer.
- Population firing rate: Average population instantaneous firing rate for one layer, computed with a time window of 25 ms. For both

AMPAR density and population firing rate, we computed the cross-correlation function between these data and the input stimulation signal (see Figures 3 and 4). To analyze the effects of conditions («*without astrocyte*» and «*with astrocyte*») on these data, we fitted a linear mixed model (LMM) on the maximal points of each correlation. For firing rate and AMPAR density correlation with the signal pattern, we kept the best correlation coefficient and the lag at which it is observed. The LMM estimated the fixed effect for the simulation conditions («*without astrocyte*» and «*with astrocyte*»), the switching frequency of the input signal pattern, the neuronal layer, and the neuron type (excitatory and inhibitory). The LMM also estimated the random effect for each simulation combination by condition by switching frequency (i.e., run(30) $\times$ condition(2) $\times$ switching frequency(9) $=$ 540 individuals).

- Transfer function: The transfer function was computed using the average population input instantaneous firing rate and the corresponding population output instantaneous firing rate. Then we fitted a least-square polynomial on the data collected.
- Astrocytic activity: The astrocytic activity was binarized and averaged over the layer's population. That is, we counted 1 for all astrocytes over the gliotransmission threshold (see Table 4), otherwise 0. Then, for each recorded time point, we averaged by layer the number of astrocytes in the gliotransmission's state.

3 Results

3.1 Activity: Neuronal's Firing Rate and Signal Pattern Correlation. The higher-order interaction of the LMM (simulation condition, «*switch frequency*», layer, neuron type; see section 2.9) is not significant ($p = .075$). However, we performed a post-hoc analysis (Tukey's honestly significant difference, HSD; Tukey, 1977) to spot significant differences in the simulation condition. The significant differences are highlighted with stars (*) on Figure 5. Our main results are that neuronal activity in the network «*without astrocyte*» is often more correlated with the input signal pattern than in the network «*with astrocyte*». More specifically, the maximum correlation coefficient decreases in the condition «*with astrocyte*», which is significant for lower switching frequency, up to 3.2 Hz. For excitatory neurons, these differences arise for layers 2 and 3, while for inhibitory neurons, it appears at all layers. The latter differences are presumably due to the synaptic connectivity for inhibitory neurons, which connect only to the same population's neurons (see section 2.6). We fitted the same model on the lag at which the maximum correlation coefficients occur. However, it did not provide any significant results, meaning that there are no significant differences involving time for these correlation coefficients.

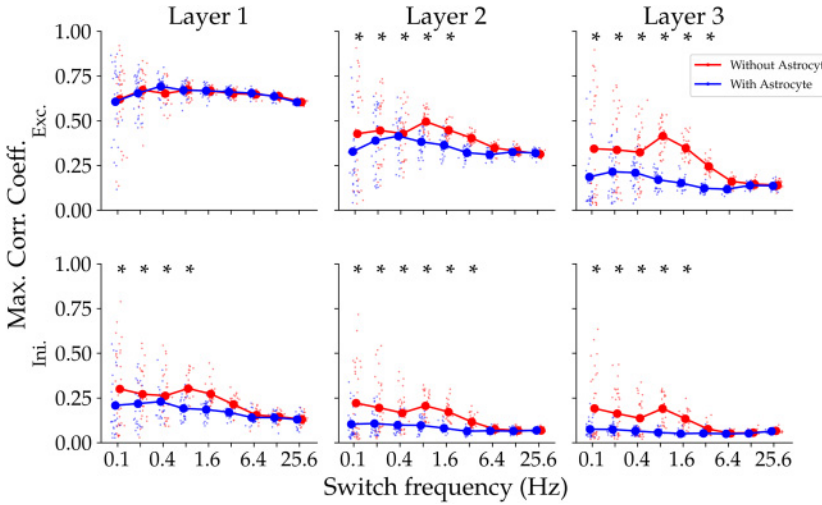

Figure 5: Maximum correlation coefficients between firing frequency and signal pattern, by simulation condition and «*switch frequency*». Top panels are excitatory neurons (Exc.); bottom panels are inhibitory neurons (Ini.). Stars (*) indicate a significant difference between the simulation condition.

3.2 Plasticity: AMPAR Trafficking and Signal Pattern Correlation. The higher interaction of the LMM (simulation condition, «*switch frequency*», layer, neuron type; see section 2.9) is not significant ($p = .36$). In the same way as section 3.1, we performed a post-hoc analysis (Tukey's HSD) to spot significant differences in the simulation conditions, displayed in Figure 6. The significant differences do not underline a strong tendency in impairing or increasing the correlation coefficient regarding the simulation conditions («*without astrocyte*» or «*with astrocyte*»). However, as displayed in Figure 6, differences arose only for the lowest switch frequencies in the signal pattern. These differences are slightly in favor of a higher correlation coefficient in the «*with astrocyte*» condition. As in the previous section, we fitted the same model on the lag at which the maximum correlation coefficients occur. It did not provide any significant results.

3.3 Discussion. These two results show that astrocyte influence leads to decorrelate neuronal activity from the input signal pattern. The correlation coefficients displayed in Figure 7 support this idea. In panels a («*without astrocyte*») and b («*with astrocyte*»), the correlation between the neuronal firing rate and the signal pattern tends to fade across the layers. The decrease of the correlation coefficient through the layer is higher for the «*with astrocyte*» condition. However, as depicted in panel c (neuronal firing rate and astrocyte activity correlation), the higher correlation coefficient at negative

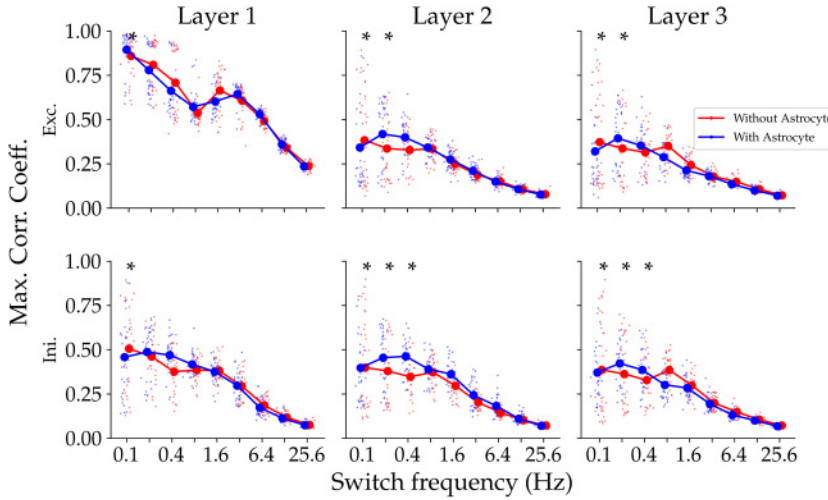

Figure 6: Maximum correlation coefficients between AMPAR density expression and signal pattern, by simulation condition and «*switch frequency*». Top panels are excitatory neurons (Exc.); bottom panels are inhibitory neurons (Ini.). Stars (*) indicate a significant difference between the simulation condition.

lag (meaning that neuronal activity precedes astrocyte activity) at lower «*switch frequency*» in the first layer tends to vanish through the layer. In the second and third layers, correlation coefficients increase around zero lag for all switching frequency. The latter modulation highlights a low-frequency modulation of astrocytic activity on neuronal processing. The same effect seems to appear in panel d (AMPAR density expression and astrocyte activity correlation), with a slightly higher amplitude. The lack of significant differences between the simulation condition (see Figure 6), for AMPAR density expression, could be due to the high-frequency dynamics of AMPAR expression (see section 2.3).

Furthermore, Figure 8 underlines a sustained transfer function through the layer in the «*with astrocyte*» condition, while it tends to fade for higher rates in the «*without astrocyte*» condition. As it does not seem to be the same for inhibitory neurons' transfer function (see Figure 9), we could conclude that astrocyte-induced modulation of the transfer function mainly affects the interneuronal population signaling, as excitatory and inhibitory neurons do not share the same connectivity pattern (see section 2.6).

The analysis of astrocytic activity confirms that astrocytes are more attuned to low-frequency varying signals. For high-frequency varying signals, the astrocytic activity is mostly decorrelated (see Figure 7e). These results are congruent with previous studies showing astrocytes' attunement

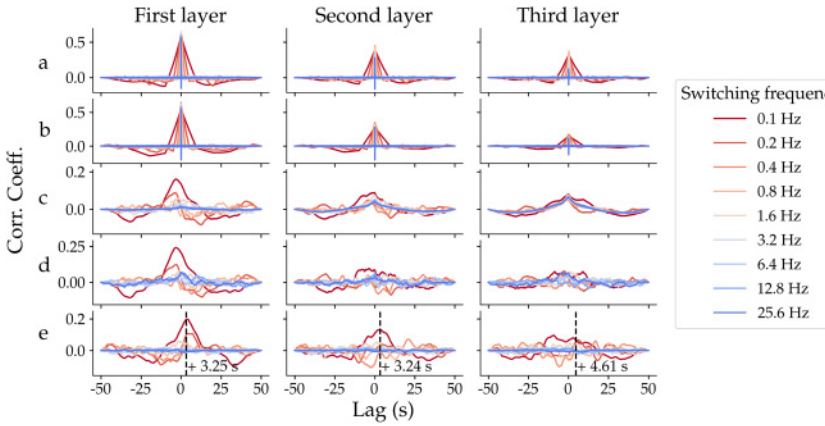

Figure 7: (a) «*without astrocyte*» mean correlation coefficient of the neuronal's firing rate (excitatory and inhibitory) with the input signal pattern. (b) «*with astrocyte*» mean correlation coefficient of the neuronal's firing rate (excitatory and inhibitory) with the input signal pattern. (c) neuronal's firing rate (excitatory and inhibitory) mean correlation coefficient with the astrocytic activity. (d) AMPAR density expression's mean correlation coefficient with the astrocytic activity. (e) Astrocytic activity (see section 2.9) mean correlation coefficient with the input signal pattern. The dashed line indicates the lag of higher correlation coefficients average.

to low-frequency activity (Perea et al., 2016; Sardinha et al., 2017). Furthermore, it confirms that the astrocytic activity is better correlated to the low-varying input signals' variations, around 2 to 4 seconds of positive lags, which is consistent with Kastanenka et al.'s (2020) observations.

4 Conclusion

In this study, we addressed the recent problem of gliotransmission influence on synaptic plasticity and neuronal activity. Recent studies show that astrocytes are critical players in extrasynaptic activity (Papouin & Oliet, 2014). The influence of gliotransmission, discussed in Pittà (2020), is that astrocytes can modulate the inductions of long-term potentiation (LTP) and long-term depression (LTD).

The neural activity in «*with astrocyte*» condition is less correlated with the input signal pattern than in the «*without astrocyte*» condition. However, the correlation increases with astrocyte activity as it decreases with the signal pattern, which leads the neuronal activity in the «*with astrocyte*» condition to be correlated with both the signal pattern and the astrocytic activity. In artificial intelligence, the artificial neural network (ANN) parameters are

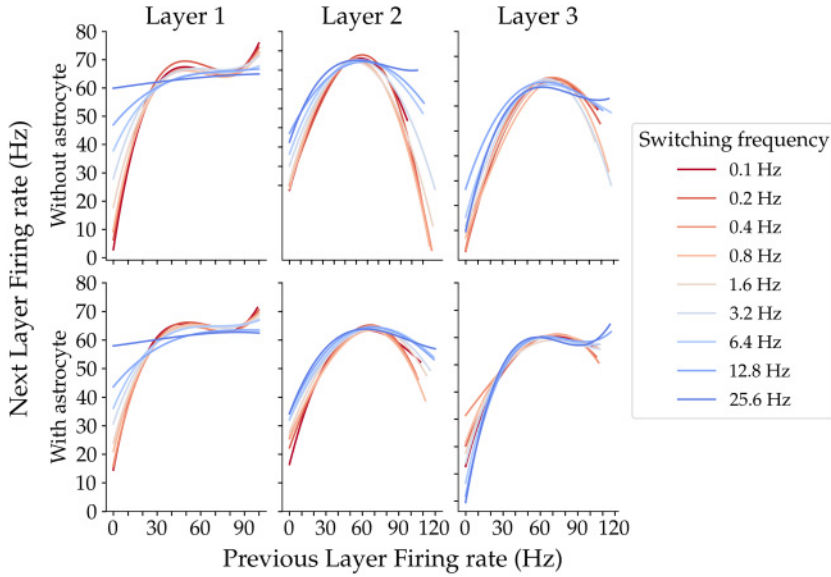

Figure 8: Excitatory neuron's average transfer function by layer and «*switch frequency*» condition.

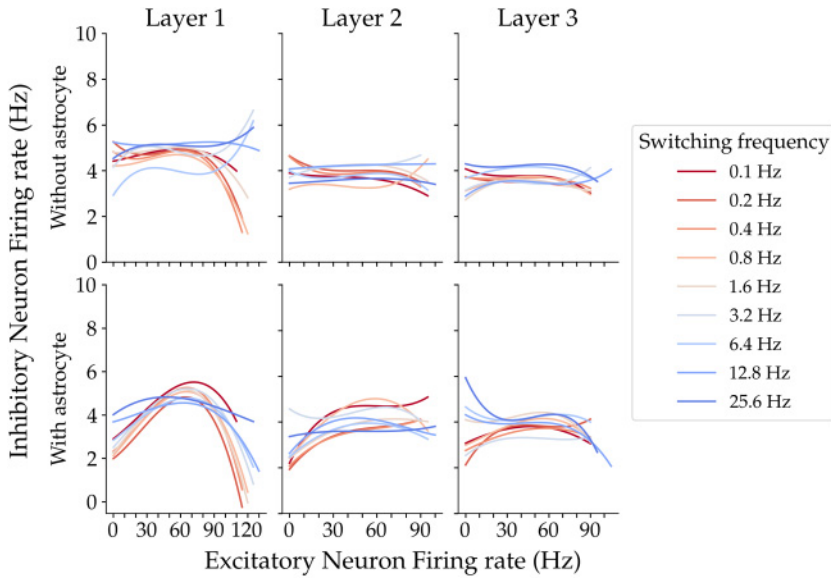

Figure 9: Inhibitory neuron's average transfer function by layer and «*switch frequency*» condition.

adjusted through backpropagation algorithms to perform computational tasks (e.g., classification, autoassociation). The transformation between the input stimulus and the ANN's output could be compared to the decorrelation between neuronal activity and the input signal pattern through the layers. The fact that astrocyte activity transforms the neuronal activity would match the trained AI processing. As astrocytes are characterized by slow dynamics, our results mean that astrocytic activity induces a low-frequency modulation of neuronal activity. This result is consistent with a recent hypothesis by Kastanenka et al. (2020), in which the authors are interested in the role that astrocytes could play in complex cognitive functions. The astrocytic low-frequency modulation of neuronal activity could link several sessions of brief information processing in time.

One limitation that arises from our results is the low correlation between the signal pattern and the data (see Figure 7). We believe that their amplitude is mainly due to the relatively small number of neurons and astrocytes in our simulation (i.e., 100 per layer; see section 2.6). However, simulations with a larger population would drastically increase the computational cost and storage capability as well. To perform such simulation at a larger scale would require adapting from other work, such as the study of Lenk et al. (2020), which should scale better with a larger population. Nonetheless, the paired comparison of «*without astrocyte*» and «*with astrocyte*» conditions (see section 2.8) provides a strong indication on the astrocytic modulation of neuronal activity and plasticity. Though some of these results could at first appear contradictory to previous studies, they complete them by extending the study of a neuron-astrocyte network in complex signal processing.

As previously investigated by Alvarellos-González et al. (2012) and Sajedinia & Hélie (2018), there is a computational gain of a neuron-astrocyte network in AI tasks. In this study, we focused on only the fast-varying plasticity (i.e., AMPAR density expression). The influence of long-term plasticity on complex signal processing is a topic that needs study. NMDAR trafficking at the synaptic and extrasynaptic locations would be much slower than AMPAR trafficking. Still, under the influence of the low-frequency astrocytic activity, it could induce an activity pattern through long time-scales. The network would display consistent activity patterns in similar conditions, distant in times, similarly to the generalization tasks in AI.

This approach would lead to a better understanding of astrocyte involvement and contribution to higher cognitive tasks.

Although we did not model all astrocytic influences (e.g., presynaptic and purinergic signaling, potassium buffering), these results again underline that astrocytes could play a decisive role in neuronal activity and, by extension, cognition. Future studies should focus on the dynamics of astrocytes at defined activity patterns to measure their influence over the neuronal activity on a large scale. Furthermore, they should include modulation of the extrasynaptic NMDAR expression to study how astrocytic activity modulates the neuronal processing. These approaches could include

different neuronal states as simulation conditions, such as wake and sleep states of neuronal activity.

References

Abbott, L. F., & Nelson, S. B. (2000). Synaptic plasticity: Taming the beast. *Nature Neuroscience*, *3*, 1178–1183.

Alvarellos-González, A., Pazos, A., & Porto-Pazos, A. B. (2012). Computational models of neuron-astrocyte interactions lead to improved efficacy in the performance of neural networks *Computational and Mathematical Methods in Medicine*, *2012*, 476324. doi:10.1155/2012/476324.

Bushong, E. A., Martone, M. E., Jones, Y. Z., & Ellisman, M. H. (2002). Protoplasmic astrocytes in CA1 Stratum radiatum occupy separate anatomical domains. *Journal of Neuroscience*, *22*, 183–192. doi:10.1523/JNEUROSCI.22-01-00183.2002.

Dayan, P., & Abbott, L. (2001). *Theoretical neuroscience: Computational and mathematical modeling of neural systems*. Cambridge, MA: MIT Press,

Delorme, A., Gautrais, J., van Rullen, R., & Thorpe, S. (1999). Spikenet: A simulator for modeling large networks of integrate and fire neurons. *Neurocomputing*, 26–27, 989–996. https://doi.org/10.1016/S0925-2312(99)00095-8.

De Pittà, M., Brunel, N., & Volterra, A. (2016). Astrocytes: Orchestrating synaptic plasticity? *Neuroscience*, *323*, 43–61. doi:10.1016/j.neuroscience.2015.04.001.

De Pittà, M., Goldberg, M., Volman, V., Berry, H., & Ben-Jacob, E. (2009). Glutamate regulation of calcium and ip3 oscillating and pulsating dynamics in astrocytes. *Journal of Biological Physics*, *35*, 383–411. doi:10.1007/s10867-009-9155-y.

De Pittà, M., Volman, V., Berry, H., & Ben-Jacob, E. (2011). A tale of two stories: Astrocyte regulation of synaptic depression and facilitation. *PLOS Computational Biology*, *7*, 1–18. doi:10.1371/journal.pcbi.1002293.

Destexhe, A., Mainen, Z., & Sejnowski, T. (1998). *Kinetic models of synaptic transmission*. Cambridge, MA: MIT Press.

Fiala, J. C., Spacek, J., & Harris, K. M. (1999). Dendrite structure. In G. Stuart, N. Spruston, & M. Husser (Eds.), *Dendrites* (2nd ed.). New York: Oxford University Press.

Flanagan, B., McDaid, L., Wade, J., Wong-Lin, K., & Harkin, J. (2018). A computational study of astrocytic glutamate influence on postsynaptic neuronal excitability. *PLOS Computational Biology*, *14*, 1–25. doi:10.1371/journal.pcbi.1006040.

Goldberg, M., De Pittà, M., Volman, V., Berry, H., & Ben-Jacob, E. (2010). Nonlinear gap junctions enable long-distance propagation of pulsating calcium waves in astrocyte networks. *PLOS Computational Biology*, *6*, 1–14. doi:10.1371/journal.pcbi.1000909.

Izhikevich, E. M. (2003). Simple model of spiking neurons. *IEEE Transactions on Neural Networks*, *14*, 1569–1572.

Jahr, C., & Stevens, C. (1990). Voltage dependence of NMDA-activated macroscopic conductances predicted by single-channel kinetics. *Journal of Neuroscience*, *10*, 3178–3182. doi:10.1523/JNEUROSCI.10-09-03178.1990.

Kastanenka, K. V., Moreno-Bote, R., De Pittà, M., Perea, G., Eraso-Pichot, A., Masgrau, R., . . . Galea, E. (2020). A roadmap to integrate astrocytes into systems neuroscience. *Glia 68*, 5–26. doi:10.1002/glia.23632.

Keller, D. X., Franks, K. M., Bartol, Jr., T. M., & Sejnowski, T. J. (2008). Calmodulin activation by calcium transients in the postsynaptic density of dendritic spines. *PLOS One*, *3*, 1–16. doi:10.1371/journal.pone.0002045.

Kepecs, A., & Raghavachari, S. (2002). Three state neurons for contextual processing. In T. G. Dietterich, S. Becker, & Z. Ghahramani (Eds.), *Advances in neural information processing systems*, *14* (pp. 229–236). Cambridge, MA: MIT Press.

Lallouette, J., De Pittà, M., & Berry, H. (2019). Astrocyte networks and intercellular calcium propagation. In M. De Pittà & H. Berry (Eds.), *Computational glioscience* (pp. 177–210). Cham: Springer.

Lenk, K., Satuvuori, E., Lallouette, J., Ladrón-de Guevara, A., Berry, H., & Hyttinen, J. A. K. (2020). A computational model of interactions between neuronal and astrocytic networks: The role of astrocytes in the stability of the neuronal firing rate. *Frontiers in Computational Neuroscience*, *13*, *92*. doi:10.3389/fncom.2019.00092.

Li, Y., & Rinzel, J. (1994). Equations for InsP3 receptor-mediated [Ca2+](i) oscillations derived from a detailed kinetic model: A Hodgkin-Huxley like formalism. *Journal of Theoretical Biology, 166*, 461–473. doi:10.1006/jtbi.1994.1041.

Lorenzo, J., Vuillaume, R., Binczak, S., & Jacquir, S. (2020). Spatiotemporal model of tripartite synapse with perinodal astrocytic process. *Journal of Computational Neuroscience*, *48*(1), 1–20. doi:10.1007/s10827-019-00734-4.

Malenka, R. C., & Bear, M. F. (2004). LTP and LTD: An embarrassment of riches. *Neuron*, *44*, 5–21. doi:10.1016/j.neuron.2004.09.012.

Morita, D., Rah, J. C., & Isaac, J. T. R. (2013). Incorporation of inwardly rectifying AMPA receptors at silent synapses during hippocampal long-term potentiation. *Philosophical Transactions of the Royal Society B: Biological Sciences*, *369*, 20130156. doi:10.1098/rstb.2013.0156.

Morris, R. (1999). D. O. Hebb: The organization of behavior, Wiley: New York; 1949. *Brain Research Bulletin*, *50*, 437. https://doi.org/10.1016/S0361-9230(99)00182-3.

Papouin, T., & Oliet, S. H. R. (2014). Organization, control and function of extrasynaptic NMDA receptors. *Philosophical Transactions of the Royal Society B: Biological Sciences*, *369*. doi:10.1098/rstb.2013.0601.

Perea, G., Gómez, R., Mederos, S., Covelo, A., Ballesteros, J. J., . . . Araque, A. (2016). Activity-dependent switch of GABAergic inhibition into glutamatergic excitation in astrocyte-neuron networks. *eLife*, *5*, e20362. doi:10.7554/eLife.20362.

Perea, G., Navarrete, M., & Araque, A. (2009). Tripartite synapses: Astrocytes process and control synaptic information. *Trends in Neurosciences*, *32*, 421–431. doi:10.1016/j.tins.2009.05.001.

Pittà, M. D. (2020). *Neuron-glial interactions.* arXiv:2001.06881.

Sabatini, B., & Svoboda, K. (2000). Analysis of calcium channels in single spines using optical fluctuation analysis. *Nature*, *408*, 589–593. doi:10.1038/35046076.

Sajedinia, Z., & Hélie, S. (2018). A new computational model for astrocytes and their role in biologically realistic neural networks. *Computational Intelligence and Neuroscience*, *2018*, 1–10. doi:10.1155/2018/3689487.

Sardinha, V. M., Guerra-Gomes, S., Caetano, I., Tavares, G., Martins, M., Reis, J. S., . . . Oliveira, J. F. (2017). Astrocytic signaling supports hippocampal–prefrontal theta synchronization and cognitive function. *Glia*, *65*, 1944–1960. doi:10.1002/glia.23205.

Scemes, E., & Giaume, C. (2006). Astrocyte calcium waves: What they are and what they do. *Glia*, *54*, 716–725. doi:10.1002/glia.20374.

Schneggenburger, R., Tempia, F., & Konnerth, A. (1993). Glutamate- and AMPA-mediated calcium influx through glutamate receptor channels in medial septal neurons. *Neuropharmacology*, *32*, 1221–1228. https://doi.org/10.1016/0028-3908(93)90016-V.

Shouval, H. Z., Castellani, G. C., Blais, B. S., Yeung, L. C., & Cooper, L. N. (2002). Converging evidence for a simplified biophysical model of synaptic plasticity. *Biological Cybernetics*, *87*, 383–391. doi:10.1007/s00422-002-0362-x.

Shuai, J. W., & Jung, P. (2002). Stochastic properties of Ca2+ release of inositol 1,4,5-trisphosphate receptor clusters. *Biophysical Journal*, *83*, 87–97. doi:10.1016/S0006-3495(02)75151-5.

Sochivko, D., Pereverzev, A., Smyth, N., Gissel, C., Schneider, T., & Beck, H. (2002). The CaV2.3 Va2+ channel subunit contributes to R-type Ra2+ currents in murine hippocampal and neocortical neurones. *Journal of Physiology*, *542*, 699–710. doi:10.1113/jphysiol.2002.020677.

Stimberg, M., Brette, R., & Goodman, D. F. (2019). Brian 2, an intuitive and efficient neural simulator. *eLife 8*, e47314. doi:10.7554/eLife.47314.

Stimberg, M., Goodman, D. F. M., Brette, R., & Pittà, M. D. (2019). *Modeling neuron–glia interactions with the Brian 2 simulator*. Cham: Springer.

Tewari, S., & Majumdar, K. (2012). A mathematical model for astrocytes mediated LTP at single hippocampal synapses. *Journal of Computational Neuroscience*, *33*, 341–370. doi:10.1007/s10827-012-0389-5.

Tolhurst, D., Movshon, J., & Thompson, I. (1981). The dependence of response amplitude and variance of cat visual cortical neurones on stimulus contrast. *Experimental Brain Research*, *41*. doi:10.1007/BF00238900.

Tukey, J. W. (1977). *Exploratory data analysis*. Reading, MA: Addison-Wesley.

Wallach, G., Lallouette, J., Herzog, N., De Pittà, M., Jacob, E. B., Berry, H., & Hanein, Y. (2014). Glutamate mediated astrocytic filtering of neuronal activity. *PLOS Computational Biology, 10*, 1–19. doi:10.1371/journal.pcbi.1003964.

Werner, G., & Mountcastle, V. B. (1965). Neural activity in mechanoreceptive cutaneous afferents: Stimulus-response relation, Weber functions, and information transmission. *Journal of Neurophysiology*, *28*, 359–397. doi:10.1152/jn.1965.28.2.359.

Wright, A., & Vissel, B. (2012). The essential role of AMPA receptor GluR2 subunit RNA editing in the normal and diseased brain. *Frontiers in Molecular Neuroscience*, *5*. doi:10.3389/fnmol.2012.00034.

Received August 27, 2020; accepted February 16, 2021.